Machine learning-based diffractive image analysis with subwavelength resolution

Abantika Ghosh[1#], Diane J. Roth[2#], Luke Nicholls[2#], William Wardley[2], Anatoly V Zayats[2], and Viktor A. Podolskiy[1*].

[1] Department of Physics and Applied Physics, University of Massachusetts Lowell, Lowell, Massachusetts 01854, USA

[2] Department of Physics and London Centre for Nanotechnology, King's College London, Strand, London, WC2R 2LS, UK

[#] Equal contributions

[*] Corresponding author: viktor_podolskiy@uml.edu

ABSTRACT: Far-field analysis of small objects is severely constrained by the diffraction limit. Existing tools achieving sub-diffraction resolution often utilize point-by-point image reconstruction via scanning or labelling. Here, we present a new technique capable of fast and accurate characterization of two-dimensional structures with at least $\lambda_0/25$ theoretical resolution, based on a single far-field intensity measurement. Experimentally, we realized this technique resolving the smallest-available to us 180-nm-scale features with 845-nm laser light, reaching a resolution of $\lambda_0/5$. A comprehensive analysis of machine learning algorithms was performed to gain insight into the learning process and to understand the flow of sub-wavelength information through the system. Image parameterization, suitable for diffractive configurations and highly tolerant to random noise was developed. The proposed technique can be applied to new optical characterization tools with high spatial resolution, fast data acquisition and artificial intelligence, such as high-speed nanoscale metrology and quality control, and can be further developed to high-resolution spectroscopy

KEYWORDS: subwavelength resolution, machine learning, diffraction, image classification, metasurfaces, scattering

Optical characterization of an object implies transferring information about its shape and spectrum to the observer via electromagnetic waves and the resolution is determined by the diffraction limit[1-6]. Existing tools achieving sub-diffraction resolution rely on resonances to compensate or postpone exponential decay of evanescent radiation[7-12] or operate on extremely sparse, often luminescent, objects to achieve point-by-point image reconstruction[13-19], typically, with multiple measurements per point. The environment separating the object and the detector determines the dispersion laws of the wave propagation and, therefore, plays a crucial role in limiting the quantity of information that can be relayed by optical means[4]. When the objects are large and well-isolated, optical systems operating in the ray-optics limit efficiently generate their images across the image plane. This regime is well-suited for a multitude of rapidly emerging computer vision technologies[21-23] that generally rely on image segmentation followed by object detection and classification. Since edge detection is used throughout the computer vision workflow, sharp edges of well-separated objects are crucial for reliable operation of machine vision.

Unfortunately, existing machine vision techniques are not readily applicable to highly diffractive configurations. Importantly, while computer vision tools increasingly use deep learning techniques with ever improving results, the exact information used by the algorithms to classify the images often remains unclear, making it almost impossible to correct the few, but important, misclassifications and predict the potential pitfalls. As the object size or separation are decreased, the deviations from ray optics due to diffraction become increasingly important, merging the images of multiple objects together and virtually eliminating the ability to resolve and identify small or closely spaced objects. Existing techniques to detect and classify small objects, including scanning optical microscopy, superlensing, structured illumination microscopy, fluorescent microsocopies, and sparsity-related super-resolution imaging typically rely on multiple measurements or reconstruct complex objects one point at a time[6-13]. However, when an object is positioned in the vicinity of a diffractive structure, light scattered by such a system carries substantial information about the object itself [24-26]. For one-dimensional objects and gratings, this information can be extracted analytically[27]. Similarly, the light scattered by a thin quasi-two-dimensional object positioned close to a two-dimensional diffractive structure carries the information about the object to the far field. However, since the increase in dimensionality necessarily yields exponential increase in complexity, the algorithms developed with line objects in mind cannot be directly applied to two-dimensional systems. Machine-learning tools, however, are implicitly robust in their ability to analyze complex patterns.

Here we demonstrate that artificial intelligence based on supervised learning can robustly classify the structure of the diffractive objects with deep-subwavelength features based on properly parameterized far-field images. The developed technique employs the diffraction of light by a finite-size grating to boost the resolution of object characterization, resolving up to $\lambda_0/25$ features of the object, with a single, noise tolerant, plane-wave-based, intensity measurement. This novel diffractive imaging approach provides a major speedup in characterization of small-scale features as compared with existing techniques, does not require scanning or multiple exposures, and can be further developed to high-resolution spectroscopy and new computer-assisted microscopy.

Diffractive signatures of subwavelength objects

We illustrate the capabilities of the proposed imaging paradigm by identifying the structure of a series of objects with subwavelength features coupled to finite diffraction gratings with lateral periods $\Lambda_x = 303 \pm 2$ nm, $\Lambda_y = 335 \pm 2$ nm, with the individual elliptical openings of short axis r_x =83 ± 2 nm and long axis r_y =90 ± 2 nm. To mimic the behavior of small objects of complex shape that block the propagation of light through some of the grating openings, we used focused ion-beam-milling (see Methods) to fabricate a series of diffractive objects (summarized in Fig. 1 and in Methods). The structures were characterized using laser light with free- space wavelengths of $\lambda_0 = 532$ nm and 845 nm (note that $r_{x,y} \simeq \lambda_0/10$), through the Fourier-optics-based diffractive imaging system (see Methods). The images recorded by the CCD camera were then post-processed to remove the background noise and suppress the contributions of the main diffraction maxima. The resulting images are shown in Fig. 1. The overall structure of these images is typical of a finite-size periodic grating. In particular, images corresponding to $\lambda_0 = 532$ nm exhibit the two main maxima representing the zero- and first-order diffraction grating peaks with their separation being proportional to the inverse period of the grating (zero-order diffraction maximum is partially obscured by the lens glare). Images corresponding to $\lambda_0 = 845$ nm exhibit one main (zero-order) diffraction peak. The positions and intensities of the auxiliary maxima represent the finer-scale structure of the grating, such as the number of openings, and the relative transparencies of individual openings.

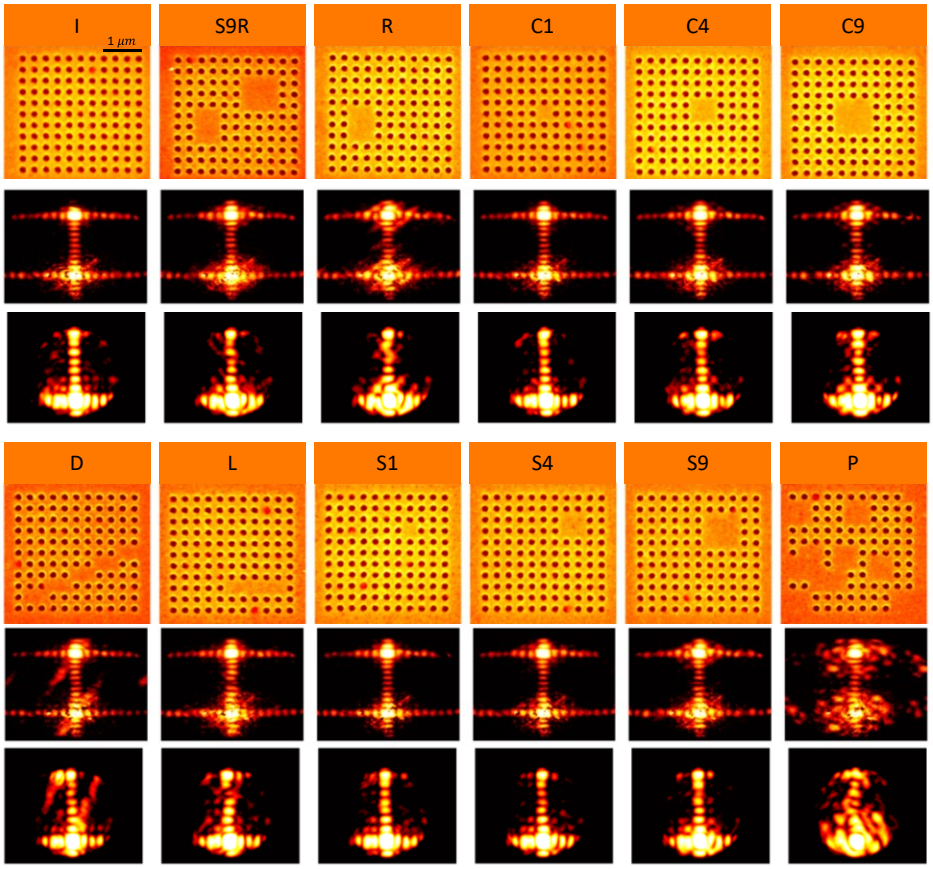

Figure 1. SEM images of the of the objects in the study (top sets) and post-processed diffraction imaging signatures of these objects for incident wavelength $\lambda_0 = 532$ nm (middle sets) and $\lambda_0 = 845$ nm (bottom sets). Nomenclature of the objects is given in Table 1. The full set of 14 samples contains two samples I and two samples L.

In general, diffraction theory can be used to predict the pattern produced by a given structure. However, the inverse problem of identifying the structure of the grating based on the pattern at hand is a rather difficult one. It is clearly seen that while some diffractive images, for example, those of the objects P and D, produce signatures that are

easily identifiable by the naked eye, the differences between the signatures produced by the majority of the samples are rather subtle. Artificial intelligence can accomplish the task of classification and identification of these complex image patterns.

In order to recognize the complex patterns that pertain to the particular objects, the AI system needs to be trained. The training set should mimic the experimental conditions and should convey the difference between experimental imperfections (i.e., abnormally sized or slightly moved opening) and an object completely blocking the particular set of openings. With this goal in mind, we digitally generated the training set of images. To produce the resulting library of diffractive signatures, the position and size of the holes in the theoretically-generated (phantom) gratings were randomly varied, with variations in position and radius of individual opening, aiming to mimic experimental conditions, as well as experimental noise. For each object in the study 100 phantom gratings were generated. To analyze the ultimate resolution limits of the proposed diffractive imaging platform, similar image sets have been created assuming identical CCD parameters but longer operating wavelengths. In order to avoid resolution enhancement resulting from possible material resonances, we assumed that diffractive structures behave as perfectly opaque screens with perfectly transparent openings. As expected, the increase of the operating wavelength results in the expansion of the diffractive patterns, reducing the number of auxiliary maxima that fit within the numerical aperture of the system, and thus reducing the number of details that are available for characterizing the objects. Typical theoretical diffractive signatures of the same subset of phantom objects for different wavelengths of incoming light are illustrated in Fig. 2.

Analysis of information flow

Once the training library of images is created, the problem of identifying the subwavelength objects is reduced to image classification, a three-stage supervised learning process that involves (i) the development of the approach that maps the image to its digital signature, (ii) training a computer classifier on the signatures of known objects, and finally (iii) the utilization of the trained classifier to identify (classify) unknown images based on their digital signatures. Note that once the classifier is trained, the actual recognition process can be completed based on a single diffractive image that corresponds to the single experimental measurement.

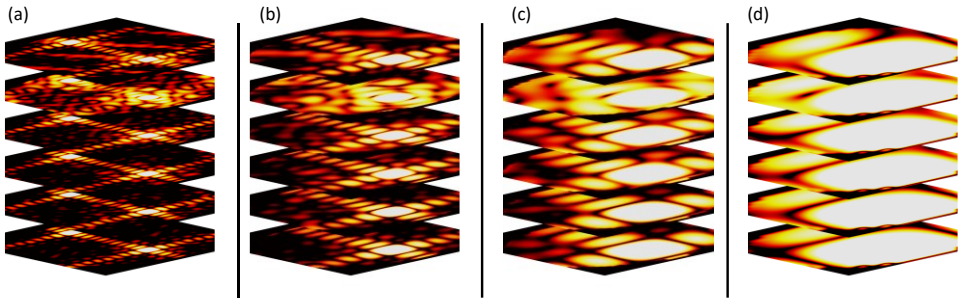

Figure 2. Diffractive signatures generated theoretically for free- space wavelength of (a) 532 nm, (b) 1 μm, (c) 2 μm, and (d) 4 μm. In each stack the images from bottom to the top represent objects I, S1, S4, R, P, and D

The first stage of this process is the most crucial one since it is responsible for optimal encoding of optical information into digital form. Conventional techniques, built with computer vision in mind, call for image segmentation, edge identification, and analysis of edge distribution within the image[28-30]. However, while sharp edges do contain a significant portion of the information in ray-optics imaging, the onset of diffraction makes edges increasingly fuzzy. In addition, unavoidable CCD noise adds parasitic edges to the complex diffractive patterns. The combination of these phenomena renders the conventional computer vision tools almost unusable for diffractive imaging and new approaches are needed.

As seen in Fig. 2, the information carried by the diffractive optical system is encoded not in the edges of the diffraction maxima but in the distribution of their position, shape, and intensity. Such information can be readily extracted when the intensity of the diffractive image distribution is represented in the Bessel transform form[31],

$$I(k_r, \phi) \simeq \sum_{m,j} C_{mj} J_m\left(\alpha_{mj} \frac{k_r}{k_0}\right) \cos(m\phi) \qquad (1)$$

where ϕ is the polar angle, α_{mj} represents the j-th zero of Bessel function $J_m(x)$, the parameters k_r and k_0 represent the radial component of the wavenumber and its maximal value, and the indices m, j describe the behavior of the intensity in the angular and radial directions, respectively (see Materials and Methods and Supporting Information [SI]). Note that since both Bessel functions and cosines form orthogonal families of functions, Eq. (1) uniquely defines the values of the coefficients C_{mj} independent of the number of terms in the sum.

In order to identify the subset of the components that carry the information about the most important features of the subwavelength objects, we utilize support vector machine (SVM)-based classifier[32-35] to analyze the library of diffractive images parameterized by a particular combination of $\{m, j\}$ pairs and analyze the accuracy of the resulting classifier as a function of the $\{m, j\}$ set. In this work, we limit

ourselves to considering subsets of the coefficients, where each of the indices $\{m, j\}$ is limited to the interval of a fixed length l (see SI for details). Typical results of such a parameter sweep are shown in Fig. 3(a-d) where each point on the diagram represents recoveries based on the set of l^2 coefficients $C_{mj} \ldots C_{m+l,j+l}$ for $l = 5$.

To produce each individual point in the dataset, the numerically generated library of the diffractive signatures was separated into the training- and testing- subsets. The SVM was trained on the training subset, and its performance was validated by classifying the diffractive signatures of the objects from the testing subset. The original library was then split into different combination of training and testing subsets and the training/validation process was repeated to gain statistical understanding of the SVM performance.

By analyzing the data (Figs. 3a-d, S3 and S4) it is seen that the lower-m ($m \lesssim 15$) harmonics are critical to accurate identification of the subwavelength features. Therefore, we conclude that the majority of information is contained in these harmonics. At the same time, as the wavelength increases the useful information shifts towards smaller j values, reflecting the slower oscillations of intensity in the radial direction with an increase of operating wavelength. Similar sweeps for larger values of parameter l, where each object is characterized by increasingly larger number of coefficients, suggest that the point of "maximum performance" approaches the origin ($m = 0, j = 1$). Combined, our analysis suggests that for best performance, the harmonics highlighted in Fig. 3(a-d) must be included in the final training and classification routines. The addition of harmonics that represent lower values of parameter j (and, thus, classify slower oscillations) may improve the results. Addition of higher-j harmonics leads to overfitting. The analysis shows that the performance of the classifiers significantly degrades only when the operating wavelength reaches $4\mu m$, almost 15 times the period of the structure, and almost 50 times the radius of an individual opening. This analysis provides a valuable insight into the dynamics underlying the machine learning process, highlighting the relative importance of different components of the image for the resulting image classification, a process that is often hidden from view in conventional image recognition systems.

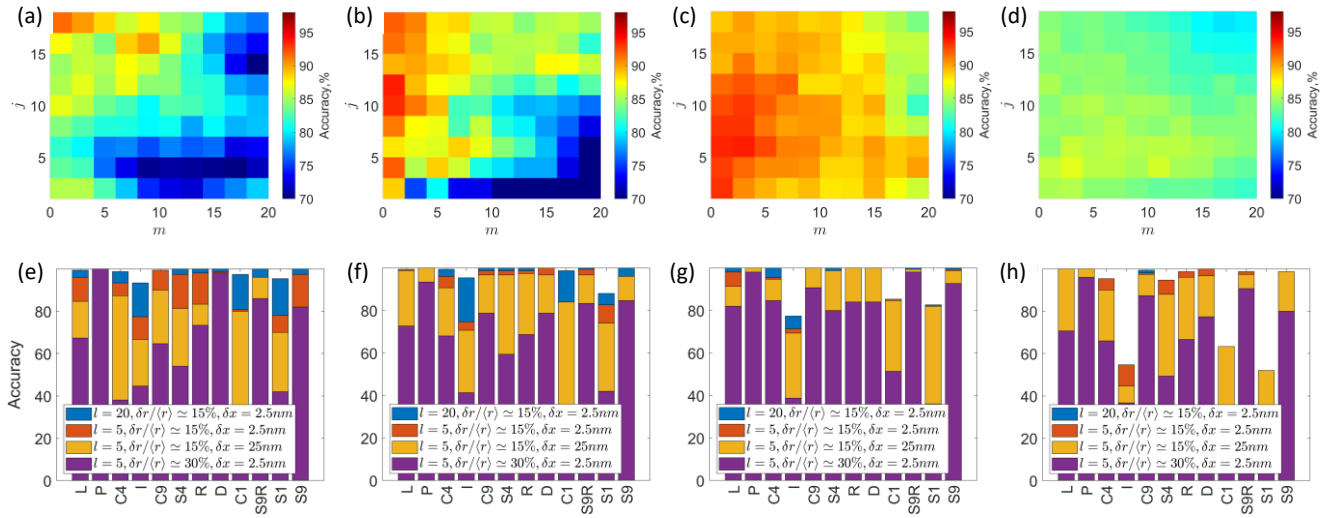

Figure 3. (a-d) Accuracy of the SVM classifiers trained on the subset of the Bessel harmonics parameterized by the set of indices $\{m, j\}$ for $l = 5$, $\delta r/\langle r\rangle = 15\%$, trained with 50 images per configuration and (e-h) classification accuracy of the particular object for different operating wavelengths: (a,e) 532 nm, (b,f) 1 μm, (c,g) 2 μm, and (d,h) 4 μm.

To test the robustness of the developed platform and to assess the effect of various parameters on its performance, the studies have been repeated with phantom sample libraries with different mean radius of individual openings $\langle r\rangle$, with different variation in radius δr, and with random point noise added to the simulated diffractive signatures. The analysis suggests that the parameters which determine the ultimate resolution represent a combination of sample-to-sample variation of geometry and the noise level. In our studies, we parameterize the geometry variations via variations in the radius of the opening δr and variations in the position of the openings δx.

To mimic the structure of the experimental samples, fabricated with focused ion beam milling, we assume $\delta x \ll \delta r$. In this limit, the mean radius of the opening, by itself, does not affect the resolution, provided that the openings are wide enough to transmit diffractive information to the far field, with the relevant dimensionless parameter that controls the accuracy of the classifier being $\delta r/\langle r\rangle$ (see SI). Figures 3,4 indicate that the algorithm is highly robust in determining the positions of the blocked openings as long as $\delta r/\langle r\rangle \lesssim 30\%$ and is also highly robust to random noise of the detector.

The variation of the position of the openings may also play significant role in the ultimate accuracy of the proposed technique (Fig. 3). Interestingly, although not surprisingly, the effect of variations in positions of the openings is strongly dependent on the wavelength. The strongest effect is observed for shorter wavelengths as can be seen from

the difference in accuracy of classification of the objects with identical δr but different δx (Fig. 3e-h).

We further analyzed the accuracy the SVM achieves in identifying each individual object by averaging the data over multiple $\{m, j\}$ realizations. As expected, not all the objects are classified with the same accuracy. Generally, the more compact (smaller) an object is, the lower its classification accuracy. We can therefore associate the scale of the smallest object to be accurately classified with the resolution of the proposed diffractive imaging technique. Based on the analysis shown in Fig. 4, the resolution limit in our study is of the order of $\lambda_0/25$ corresponding to resolving S1 object, ~150 nm in size, at $\lambda_0 = 4$ μm with 50% accuracy. However, this ideal resolution limit may be affected by various experimental factors. For example, the measured images are affected by the presence of a lens glare or CCD saturation effects, all of which can distort the diffractive information.

The performance of the classifiers is also affected by the total number of elements in the finite diffraction grating, as well as by the number of objects that are being analyzed, with larger number of holes in the gratings or larger variety of the objects yielding smaller accuracy. For example, when the number of samples is reduced from 12 to 6, accuracy of identification of remaining samples is increased by ~20 %.

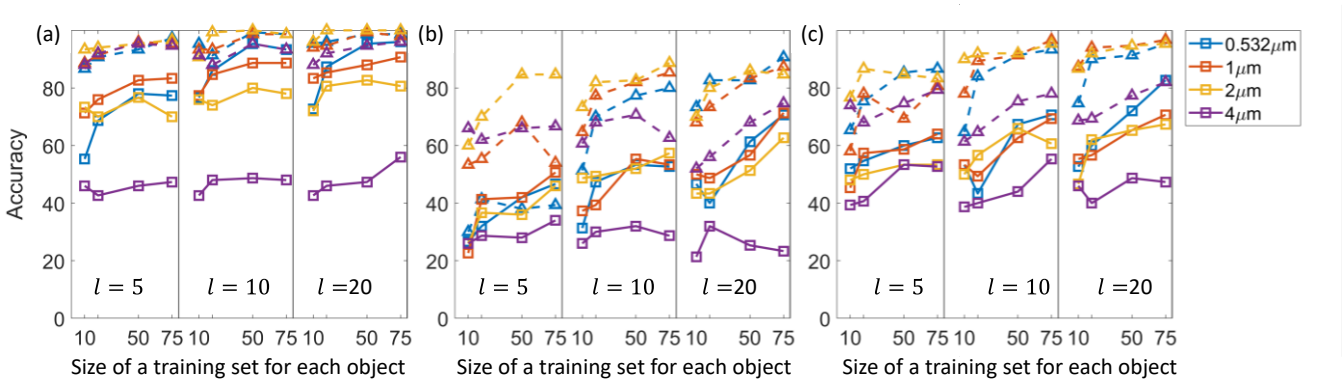

Figure 4. Classification accuracy of a testing subset as a function of the training set size for different values of the parameter l that determines the number of C_{mj} coefficients used in parameterization of each object: (solid lines) S1 object, which is the most challenging object to recover, and (dashed lines) C4 object for (a) $\delta r/\langle r\rangle \approx 15\%$ using a full set of 12 objects, and (b,c) $\delta r/\langle r\rangle \approx 30\%$ using (b) a full set of 12 objects, and (c) a shortened set of 6 objects [I,R,C4,D,S1,P].

The size of the training set is an important parameter in the analysis of the performance of any AI-based system. Conventional ray-optics machine vision systems often require millions of training images to properly train a deep learning network. Recent theoretical studies of applications of convolutional neural networks to subwavelength imaging[36] confirm these trends, requiring $\sim 2 \times 10^4$ training sets and multiple "measurements" of both field amplitude and phase to resolve the dimensions and a separation between two 1D linear objects. Increase of dimensionality as well as limitation of intensity-based imaging tend to further increase the complexity of recovery algorithms and decrease the resulting resolution[4,26]. In contrast, the training process for the SVM-based 2D diffractive imaging is rather efficient, with only ~50 representations of each object being enough to ensure classification accuracy of above 50% for even the *worst-case*- S1 object for $\lambda_0 \leq 4$ μm, based on a single far-field diffractive intensity pattern (Fig. 4). Classification of larger objects is even more robust, with ~20 representations of each object being enough to achieve 80% accuracy for $\lambda_0 \leq 4$ μm.

Experimental realization of diffractive image analysis

We now apply the developed formalism to classify the objects fabricated experimentally. In order to more comprehensively assess the perspectives of the machine-learning-based diffractive imaging, each sample was characterized with four different illumination directions, labeled here as Left, Right, Up, and Down, with data representing each direction analyzed independently and, therefore, with each classification performed based on the result of single experimental measurement. Statistical analysis of such recoveries (Fig. 5) illustrates the robustness of the developed classifier that has been trained exclusively on theory-generated data. The classifier is capable of detecting each object (with smallest available to us dimension of 180 nm) with 532 nm and 845 nm laser light wavelengths. Note that while coherent laser light has been used in this work, our previous study[27] has indicated that gratings-assisted imaging works with incandescent white-light illumination.

Similar to the theoretical studies reported above, not all the objects are classified with the same accuracy. In agreement to theory-based studies, the objects that exhibit the worst classification accuracy tend to be the smallest objects and the combination of $\{m, j\}$ indices that results in the highest accuracy being localized in the range of small m and wavelength-dependent j values. In our studies, the best accuracy of recovery of experimental images (13/14 for $\lambda_0 = 532$ nm and 12/14 for $\lambda_0 = 845$ nm, see details in SI) was achieved with classifiers trained on theoretical image sets with $\delta r/\langle r\rangle \simeq 30\%$. We note that while in the present work theory-based SVM training has been used, in practical settings where the experimental setup is used to characterize multiple similar objects (for example, on production lines),

SVMs can be trained on the diffractive signatures of known objects. Such procedure would incorporate systematic artifacts, including lens glare, CCD noise and imperfections, etc. into the training process itself.

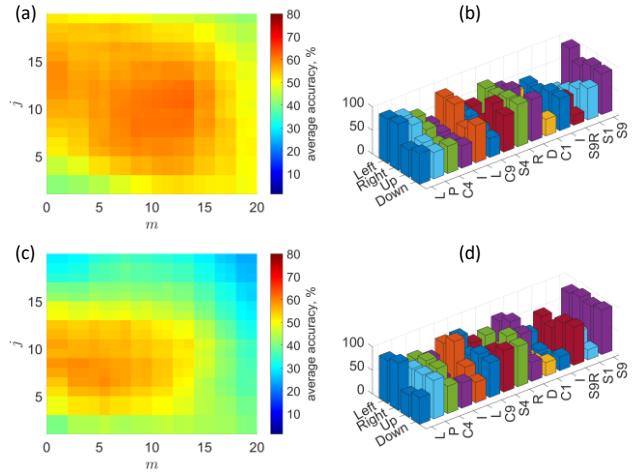

Figure 5. (a,c) The dependence of the accuracy of identification of the experimental objects in Fig. 1 for different combinations of m, j parameters, averaged over $l \in [5,10,20]$, and different classifier settings. (b,d) Accuracy of characterization of the experimental objects as a function of orientation of illumination (Left, Right, Up, Down) for a subset of data shown in (a) resulting in recoveries of more than 6 samples for operating wavelength of 532 nm (a,b) and 845 nm (c,d).

Methods

Sample fabrication

The 2-dimensional gratings were fabricated in a 100 nm thick gold film using focused ion beam milling. The gold film was deposited on a glass coverslip covered with a 15 nm tantalum pentoxide (Ta_2O_5) adhesion layer using a DC magnetron sputtering. The ideal structure, without defects, consists of an 11x11 array of elliptical holes of short axis 83 ± 2 nm and long axis 90 ± 2 nm; two ideal structures have been fabricated. The lattice periods are 303 ± 2 nm and 335 ± 2 nm in the short and long axis directions, respectively. Various geometrical defects were introduced in the fabrication of the other gratings by omitting holes, producing variations in the Fourier diffraction patterns experimentally and theoretically observed. Defects included single missing holes and square patterns of 2x2 or 3x3 missing holes, located either in the center of the array or within a first quadrant of the structure; a 2x3 rectangle; the combination of a 3x3 square and 2x3 rectangle; a diagonal line defect; a 1x5 straight line (two structures have been fabricated); as well as a complex pattern of missing holes. Each of the 12 types of objects used in the study is assigned a unique legend consisting of a (set of) letters and numbers (Table 1).

Table 1. Nomenclature of the objects shown in Fig. 1

Label	Object Description	Label	Object Description
I	Ideal grating, no intentional defects	S9R	Grating with a 9-hole square and a 6-hole rectangular area blocked
R	Grating with a 6-hole rectangular area blocked	C1	Grating with a center hole blocked
C4	Grating with a 4-hole square area in the center blocked	C9	Grating with a 9-hole square area in the center blocked
D	Grating with 8-hole oblique line blocked	L	Grating with a 5-hole horizontal line blocked
S1	Grating with a single off-center hole blocked	S4	Grating with a 4-hole off-center square area blocked
S9	Grating with a 9-hole off-center square are blocked	P	Grating with a complex pattern blocked

Optical measurements

Optical measurements were performed using the experimental setup (Fig. 6) similar to the one described in Ref. (27). The structures were illuminated by a quasi-plane-wave, generated by focusing a 532 nm CW laser beam onto the back focal plane of a 40x objective (0.95 NA) incident on the metal film. The angle of incidence on the sample was controlled by displacing the focal spot onto the back focal plane of the illumination objective. The scattered light from the structures was collected in transmission through the substrate by an oil immersion 100x objective (NA= 1.49). The back focal plane of the detection objective (Fourier plane) was then imaged onto an imaging spectrometer using a set of relay lenses.

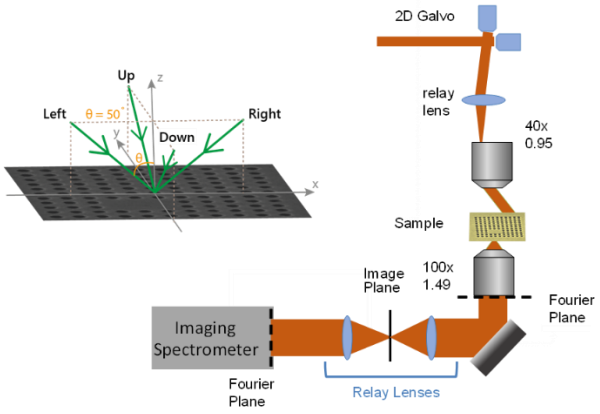

Figure 6. Optical setup for performing diffractive imaging at $\lambda_0 = 532$ nm. A similar setup was used for $\lambda_0 = 845$ nm but with a collection objective of NA=1.3. Inset shows the different orientations of illumination direction (Left, Right, Up, Down), the angle of incidence is theta=50° for all orientations

For each structure, a measurement at normal incidence from the sample was taken, along with a set of measurements at an angle of incidence of 50° for four cardinal orientations of the illumination direction (see inset in Fig. 6). The power of the laser was set to 150 μW and two sets of measurements were then recorded for exposure times of 10 ms and 40 ms, in order to collect more intensity in the higher

diffraction orders for analysis. Background images on the gold film were also recorded. The same setup was used for incident light with 845 nm wavelength, with the exception of the collection objective, replaced by an oil immersion 100x objective with NA=1.3 and the corresponding adjustment of exposure time.

Theoretical generation of library of images

Far-field (Fraunhofer) approximation is used to generate the Fourier signatures of different samples in the theoretical studies. Numerically, we begin with computer-generated binary mask representing the geometry of the particular grating, with openings randomly displaced from the "ideal" periodic grating by at most 2.5 nm, simulating the precision of the fabrication technique, and with randomly generated opening radius of $\langle r\rangle \pm \delta r$ with $\langle r\rangle \in [60\text{ nm}, 120\text{ nm}]$, and $\delta r \in [5\text{ nm}, 20\text{ nm}]$. We assume that the openings of the grating are fully transparent to the monochromatic plane wave while the space between the openings fully blocks the incoming radiation. Therefore, the spatial distribution of the electromagnetic field just behind the grating is proportional to the binary mask of the grating itself.

This spatial profile is then Fourier-transformed, and the bandwidth of the resulting Fourier representation is cut to mimic the numerical aperture of the optical setup used in the experiments. To mimic the aberration of the experimental setup, we followed the coordinate transformation $\{k_x, k_y\} \rightarrow \{k_x, k_y[1-\alpha\, k_x^2]\}$, with the value of the parameter α based on experimental images. The slight ellipticity of the holes in the experiment has been neglected as the deviations from the circular holes ($\pm$15 nm) are beyond the resolution of the proposed set-up.

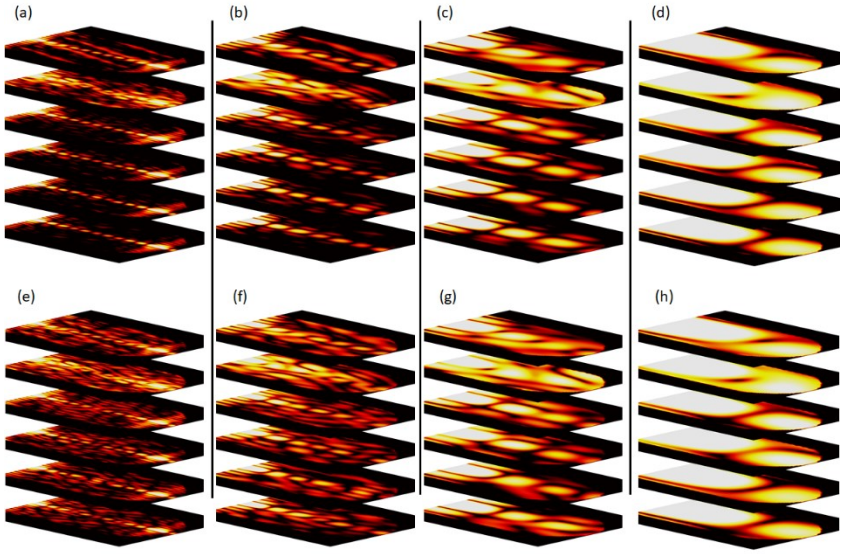

Figure 7. Diffractive signatures generated theoretically for a free space wavelength of 532 nm (a,e), 1 μm (b,f), 2 μm (c,g), and 4 μm (d,h) with $\delta r/\langle r\rangle \approx 15\%$ (a-d) and with $\delta r/\langle r\rangle \approx 30\%$ (e-h). In each stack the images represent (from bottom to top) represent objects I, S1, S4, R, P, and D, respectively

Image post-processing

Prior to machine learning analysis, each CCD image was post-processed according to the following algorithm. First, the background pattern (representing transmission through smooth gold film) was subtracted. Next, the CCD noise and the saturated signals were discarded (by imposing lower and upper cut-off values). CCD signals representing CCD space outside the numerical aperture of the imaging signal was discarded as well. Finally, the intensity was converted to the log scale to enhance the diffractive signals. Theoretically-produced intensity distributions were post-processed in similar fashion. In all analyses, only the portion of the image representing $0 \le k \le k_0, -\frac{\pi}{2} \le \phi \le \frac{\pi}{2}$ (see Eq. (1) and Fig. 7) was used.

Setup of the support vector machine

Support vector machines (SVM) implementation outlined in Ref. (32-34) was used in this work. To understand and optimize the information flow through the system, we have analyzed the recovery accuracy of multiple SVMs, with linear, polynomial, as well as Gaussian kernels, and with different multiclass classification combinations. The analysis suggests that linear kernel with the multiclass classifier that relies on the array of one vs. all binary SVM sub-classifiers performs the best for the diffractive classification problem.

In order to train and validate SVMs used in this study, the generated phantom objects were randomly partitioned into training and testing subsets. In theoretical studies, the training subset (of the length of t =10-75 images/sample) was used to train the SVM, whose accuracy was then validated based on the randomly chosen 15 of the remaining images/sample. 10 runs were performed for each m, j, l, t

combination. The accuracy derived from these calculations was consistent with k-fold estimates provided by automatic SVM training diagnostics.

In the experimental studies, the SVMs were trained based on full 100-image/sample theoretical libraries and their accuracy was calculated by analyzing the classification of the experimental signatures.

Assessing the robustness of classification in simulations

To assess the robustness of the algorithm with respect to the random noise (for example, generated by the CCD) as well as fabrication imperfections, we generated phantom libraries representing multiple combinations of parameters $\langle r \rangle$, δr, and δx. Fig. 7 illustrates the diffractive patterns representing different levels of radius variation parameterized by the parameter $\delta r/\langle r \rangle$. Noise-affected images were formed by starting with its no-noise "baseline" counterpart and adding a set of Gaussian noise spikes at random locations of the image. The level of noise is parameterized by the fraction of the total area occupied by the noise spikes. Adding particular noise to the training set can be used to model the imperfections of the particular image sensor, such as its shot noise, read-out noise or fixed pattern noise.

Conclusions and Outlook

We have demonstrated the robust classification of subwavelength objects with diffractive imaging and machine learning approach. Experimentally, smallest available to us objects of the order of $\lambda_0/5$ have been detected. Theoretical results suggest that the technique is highly tolerant to hardware noise and can be used to detect and classify smaller, at least $\sim\lambda_0/25$ objects with $\sim$50% accuracy. Apart from demonstrating the new optical characterization approach, we have developed a robust procedure for parameterization of diffractive images and identified the primary information flow channels used by the machine learning algorithms. As with any machine-learning techniques, the process of image recognition can be further optimized by providing training data that would more closely resemble experimental data with its systematic aberrations. In this sense, classification performance can be improved if realistic imaging is trained on experimental data, not on idealized theoretical predictions of known objects.

All in all, the proposed technique opens the door for robust classification and characterization of objects with subwavelength structure, including fast and robust quality control in nanofabrication, and optical analysis of nano-structural fingerprints of complex objects. The same approach can be used to analyze, in transmission geometry, the structure and the spectrum of small objects positioned above the finite diffraction gratings. In this scenario the object blocks a number of the openings of the diffraction grating and, therefore, modifies the transmission through the structure. A properly trained classifier can then be used to identify the subset of the blocked holes and thus, to recover the structural information about the object. Repeating the same process for different incident wavelength yields spectral, in addition to structural, information about the object. The proposed technique can be further extended to characterization of complex metasurfaces with resonant elements in either reflection or in transmission mode. In this case, the classifier should be trained on signatures that take into account the (geometry- and materials-dependent) optical response of the metasurface components.

ASSOCIATED CONTENT

Supporting Information
The Supporting Information is available free of charge at https://pubs.acs.org/doi/10.1021/NNNN.
Bessel transforms and object signatures, parameters affecting accuracy of the object classification, classification of experimental objects based on theoretically generated data, supplementary Figures S1-S5.

Funding Sources

The research was partially supported by the Army Research Office (US) Grant #W911NF-16-1-0261, National Science Foundation (US) Grant #IIS-2026703, EPSRC (UK), and ERC iCOMM project (789340).

References

(1) Helmholtz, H. Von On the Limits of the Optical Capacity of the Microscope. *Proceedings of the Bristol Naturalists' Society*. **1874**, 1, 435.

(2) Lord Rayleigh On the theory of optical images, with special reference to the microscope. *Philos. Mag.* **1896,** 42 (255), 167–195.

(3) Abbe, E. K. Beitrage zur Theorie des Mikroskops und der mikroskopischen Wahrnehmung. *Archiv fur mikroskopische Anatomie.* **1873**, 9(1), 413.

(4) Narimanov, E.E. Resolution limit of label-free far-field microscopy. *Adv. Photon.* **2019,** 1, 056003.

(5) Richards, D.R.; Zayats A.V. Nano-Optics and Near-Field Optical Microscopy; Artech House: Boston, 2008.

(6) Gustafsson, M. G. Surpassing the lateral resolution limit by a factor of two using structured illumination microscopy. *J. Microsc.* **2000,** 198 (2), 87.

(7) Pendry, J.B. Negative refraction makes a superlens. *Phys.Rev.Lett.* **2000,** 85, 3966.

(8) Podolskiy, V.A.; Narimanov, E.E. Near-sighed superlens. *Opt. Lett.* **2005**, 30, 75.

(9) Zhang, X.; Liu, Z. Superlenses to overcome the diffraction limit. *Nature Materials.* **2008,** 7, 435.

(10) Jacob, Z.; Alekseyev, L.; Narimanov, E. Optical hyperlens: far-field imaging beyond the diffraction limit. *Opt. Express.* **2006,** 14, 8247–8256.

(11) Salandrino; Engheta, N. Far-field subdiffraction optical microscopy using metamaterial crystals: theory and simulations. *Phys. Rev. B.* **2006**, 74, 075103.

(12) Liu, Z.; Lee, H.; Xiong, Y.; Sun, C.; Zhang, X. Far-field optical hyperlens magnifying sub-diffraction-limited objects. *Science.* **2007**, 315, 1686.

(13) Rust, M. J.; Bates, M.; Zhuang, X. Sub diffraction-limit imaging by stochastic optical reconstruction microscopy (STORM). *Nature Methods.* **2006** 3 (20), 793.

(14) Hess, S. T.; Girirajan, T. P. K.; Mason, M. D. Ultra-high resolution imaging by fluorescence photoactivation localization microscopy. *Biophys. J.* **2006,** 91, 4258–4272.

(15) Hell, W.; Wichmann, J. Breaking the diffraction resolution limit by stimulated emission: stimulated-emission-depletion fluorescence microscopy. *Opt. Lett.* **1994**, 19, 780–782.

(16) Balzarotti, F.; Eilers, Y.; Gwosch, K.; Gynn, A. H.; Westphal, V.; Stefani, F. D.; Elf, J.; Hell, S. W. Nanometer resolution imaging and tracking of fluorescent molecules with minimal photon fluxes. *Science.* **2017,** 355 (6325), 606.

(17) Rogers, E. T. F.; Lindberg, J.;Roy, T.; Savo, S.; Chad, J. E.;Dennis, M. R.;Zheludev, N. I. A super-oscillatory lens optical microscope for subwavelength imaging. *Nat. Mater.* **2012**, 11, 432.
(18) Du, L.; Yang, A.,;Zayats, A. V.; Yuan, X.-C.; Deep-subwavelength features of photonic skyrmions in a confined electromagnetic field with orbital angular momentum. *Nat. Phys.* **2019**, 15, 650.
(19) Gazit, S.; Szameit, A.; Eldar, Y. C.; Segev, M. Super-resolution and reconstruction of sparse sub-wavelength images. *Opt. Express*. **2009**, 17, 23920.
(20) Szameit, A.; Shechtman, Y.; Osherovich, E.; Bullkich, E.; Sidorenko, P.; Dana, H.; Steiner, S.; Kley, E. B.;Gazit, S.; Cohen-Hyams, T.; Shoham, S. ; Zibulevsky, M.; Yavneh, I.; Eldar, Y. C.; Cohen O.; Segev, M. Sparsity-based single-shot subwavelength coherent diffractive imaging. *Nature Materials.* **2012**, 11 (5), 455.
(21) Farabet, C.; Couprie, C.; Najman, L.; LeCun, Y. Learning Hierarchical Features for Scene Labeling. *IEEE Transactions on Pattern Analysis and Machine Intelligence*. **2013**, 35, 1915.
(22) Szeliski, R. Computer vision: Algorithms and applications; Springer: London, **2011**.
(23) Jiang, X.; Hadid, A.; Pang, Y.; Granger, E.; Feng, X., Eds.; Deep Learning in object detection and recognitionSpringer: Singapore, **2019**.
(24) Sentenac, A.; Chaumet, P.; Belkebir K. Beyond the Rayleigh criterion: grating assisted far-field optical diffraction tomography. *Phys. Rev. Lett.* **2006** 97, 243901.
(25) Thongrattanasiri, S.; Kuhta, N. A.; Escarra, M. D.; Hoffman, A. J.; Gmachl, C. F.; Podolskiy, V. A. Analytical technique for subwavelength far field imaging. *Appl. Phys. Lett.* **2010**, 97, 101103.
(26) Inampudi, S.; Kuhta, N.; Podolskiy, V. A. Interscale mixing microscopy: numerically stable imaging of wavelength-scale objects with subwavelength resolution and far field measurements. *Opt. Express.* **2015**, 23, 2753–2763.
(27) Roberts, C.M.; Olivier, N.; Wardley, W.P.; Inampudi, S.; Dickson, W.; Zayats, A.V.; Podolskiy, V.A. Interscale Mixing Microscopy: far field imaging beyond the diffraction limit. *Optica.* **2016**, 3, 803.
(28) Rosten, E.; Drummond, T. Fusing Points and Lines for High Performance Tracking. *Proceedings of the IEEE International Conference on Computer Vision.* **2005**, 2, 1508–1511.
(29) Leutenegger, S.; Chli, M.; Siegwart, R. BRISK: Binary Robust Invariant Scalable Keypoints. Proceedings of the IEEE International Conference, ICCV, **2011**.
(30) Bay, H.; Ess, A.; Tuytelaars, T.; Van Gool, L. SURF: Speeded Up Robust Features. *Computer Vision and Image Understanding (CVIU).* **2008,** 110, 346–359.
(31) Jackson, J.D. Classical Electrodynamics; John Willey and Sons: New York, 1999.
(32) Allwein, E.; Schapire, R.; Singer, Y. Reducing multiclass to binary: A unifying approach for margin classifiers. *Journal of Machine Learning Research*. **2000**, 1, 113–141.
(33) Christianini, N.; Shawe-Taylor, J. C. An Introduction to Support Vector Machines and Other Kernel-Based Learning Methods; Cambridge University Press: Cambridge, UK, 2000.
(34) Scholkopf, B.; Smola, A. Learning with Kernels: Support Vector Machines, Regularization, Optimization and Beyond, Adaptive Computation and Machine Learning; The MIT Press: Cambridge, MA, 2002.
(35) Hastie; Tibshirani, T., R.; Friedman, J. The Elements of Statistical Learning, Second Edition; Springer: NY, 2008
(36) Pu, T.; Savinov, V.; Yuan, G.; Papasimakis, N.; Zheludev, N. I. Unlabelled Far-field Deeply Subwavelength Superoscillatory Imaging (DSSI). 2019, arXiv1908:00946. arXiv.org e-Print archive.https://arxiv.org/abs/1908.00946 (accessed Aug 2, 2019)

Authors are required to submit a graphic entry for the Table of Contents (TOC) that, in conjunction with the manuscript title, should give the reader a representative idea of one of the following: A key structure, reaction, equation, concept, or theorem, etc., that is discussed in the manuscript. Consult the journal's Instructions for Authors for TOC graphic specifications.